Fine structure and dynamics of EB3 binding zones on microtubules in fibroblast cells

V. V. Mustyatsa[a,b,†], A. V. Kostarev[a,†], A. V. Tvorogova[a], F. I. Ataullakhanov[a,b,c], N. B. Gudimchuk[a,b,c], and I. A. Vorobjev[a,d,*]

[a]Lomonosov Moscow State University, 119991 Moscow, Russia; [b]Dmitry Rogachev National Research Center of Pediatric Hematology, Oncology and Immunology, 117198 Moscow, Russia; [c]Center for Theoretical Problems of Physicochemical Pharmacology, Russian Academy of Sciences, 119334 Moscow, Russia; [d]Nazarbayev University, 010000 Nur-Sultan, Kazakhstan

ABSTRACT **End-binding (EB) proteins associate with the growing tips of microtubules (MTs) and modulate their dynamics directly and indirectly, by recruiting essential factors to fine-tune MTs for their many essential roles in cells. Previously EB proteins have been shown to recognize a stabilizing GTP/GDP-Pi cap at the tip of growing MTs, but information about additional EB-binding zones on MTs has been limited. In this work, we studied fluorescence intensity profiles of one of the three mammalian EB-proteins, EB3, fused with red fluorescent protein (RFP). The distribution of EB3 on MTs in mouse fibroblasts frequently deviated from single exponential decay and exhibited secondary peaks. Those secondary peaks, which we refer to as EB3-islands, were detected on 56% comets of growing MTs and were encountered once per 44 s of EB3-RFP comet growth time with about 5 s half-lifetime. The majority of EB3-islands in the vicinity of MT tips was stationary and originated from EB3 comets moving with the growing MT tips. Computational modeling of the decoration of dynamic MT tips by EB3 suggested that the EB3-islands could not be explained simply by a stochastic first-order GTP hydrolysis/phosphate release. We speculate that additional protein factors contribute to EB3 residence time on MTs in cells, likely affecting MT dynamics.**

Monitoring Editor
Thomas Surrey
The Francis Crick Institute

Received: Nov 14, 2018
Revised: May 14, 2019
Accepted: May 21, 2019

INTRODUCTION

Many cellular processes, including cell division, migration and polarization depend on dynamic instability—a unique property of microtubules (MTs), manifesting in their spontaneous switching between phases of growth and shrinkage (Desai and Mitchison, 1997). It is currently widely accepted that dynamic instability is explained by the presence of a stabilizing cap, made of GTP-bound tubulin subunits (Bowne-Anderson *et al.*, 2013; Brouhard and Rice, 2018). While the stabilizing cap is present at the MT tip, the MT can grow. When the stabilizing cap is lost due to stochastic GTP hydrolysis, or dissociation of GTP-tubulins, or loss of lateral bonds between them, MTs switch to the shrinkage (Zakharov *et al.*, 2016). The structure and dynamics of the stabilizing cap, however, have remained elusive because of the lack of direct methods to visualize it. Special antibodies have been developed to recognize GTP-tubulins (Dimitrov *et al.*, 2008), but due to their large size and slow unbinding kinetics they did not allow dynamic study of nucleotides distribution in the MT with sufficient temporal resolution. Important insight into the MT tip came from the studies of end-binding (EB) proteins, which currently serve as the best available natural probe to study the stabilizing cap (Akhmanova and Steinmetz, 2015). EB-proteins have been shown to sense nucleotide state of tubulins and recognize the region, responsible for instantaneous MT stability in vitro (Maurer *et al.*, 2011; Duellberg *et al.*, 2016). In mammals, EB-proteins family is represented by three members, EB1, EB2 and EB3, functioning as MT dynamics modulators and a platform for recruiting many other factors to growing MT tips (Mustyatsa *et al.*, 2017). Studies in cells and on isolated MTs have demonstrated that the EB proteins decorate the tips of the MTs with a comet-like

This article was published online ahead of print in MBoC in Press (http://www.molbiolcell.org/cgi/doi/10.1091/mbc.E18-11-0723) on May 29, 2019.

†These authors contributed equally to this work.

*Address correspondence to: I. A Vorobjev (ivan.vorobyev@nu.edu.kz).

Abbreviations used: EB, end binding; MT, microtubule; RFP, red fluorescent protein.

distribution, slightly shifted from the very tip of the MT (Nakamura *et al.*, 2012; Maurer *et al.*, 2014; Roth *et al.*, 2019). Following assumption that EB-proteins recognize GTP/GDP-Pi tubulins, whose transition to GDP state is a first-order stochastic process, EB-profiles on MTs were usually averaged and approximated with a single exponential decay function to extract the characteristic comet length during MT growth phase (Bieling *et al.*, 2008; Seetapun *et al.*, 2012; Maurer *et al.*, 2014). This approach carried information about average properties of MT cap, but ignored potentially important information about its fine structure. Individual EB profiles are usually noisy, and contain additional peaks (Komarova *et al.*, 2009; Nakamura *et al.*, 2012; Mohan *et al.*, 2013), which could reflect the presence of additional EB-binding zones, containing GTP/GDP-Pi-tubulin, so called GTP/GDP-Pi remnants or islands (Dimitrov *et al.*, 2008; Aumeier *et al.*, 2016). Frequency, positions, and dynamics of these zones, which are thought to be important drivers of MT rescue, have not yet been systematically examined.

In this study, we have undertaken analysis of the shape and dynamics of EB3 distribution on growing MTs in fibroblasts with high temporal resolution. We have found that the EB3 comet length and shape remain constant on average over the MT growth phase, although fluctuate significantly. Individual distributions of EB3 along MTs often deviate from exponential shape, forming relatively long-lived EB3-islands. A well-characterized two-state kinetic model of MT dynamics (VanBuren *et al.*, 2002), modified to include EB3 decoration, failed to explain long-lived EB3-islands, suggesting that additional factors contribute to EB3 binding to MTs.

RESULTS AND DISCUSSION

EB3-profile characteristics remain relatively constant throughout EB3 comet lifetime

To study fine structure and dynamics of EB-proteins distribution on MTs in live cells, we expressed EB3 tagged with red fluorescent protein (RFP) in 3T3 mouse fibroblasts. As expected, under moderate expression level, EB3-RFP formed moving comet-like structures, which we visualized with TIRF microscopy and recorded at 5 frames/s rate (Figure 1, A and B). Kymographs of non-intersecting EB3-RFP tracks were built and analyzed (Figure 1C). Comet intensity profiles were then measured for each individual time frame of the kymographs by taking corresponding line-scans along the MT. Resulting profiles showed normalized intensity as a function of coordinate along the MT (Figure 1D), with *x*-axis pointed toward the growing tip of the MT. Following previous work, we first assumed that EB3-binding sites disappear as a first order process, so that the tail of the EB3-RFP comet should be approximated as single exponential function. The front of the comet can be approximated with a Gaussian function (Figure 1D; Eq. 1 in *Materials and Methods*). Alignment of multiple EB3-RFP profiles by the position of the maximum of the fitting function revealed that on average exponential/Gaussian function indeed described the data with a good determination

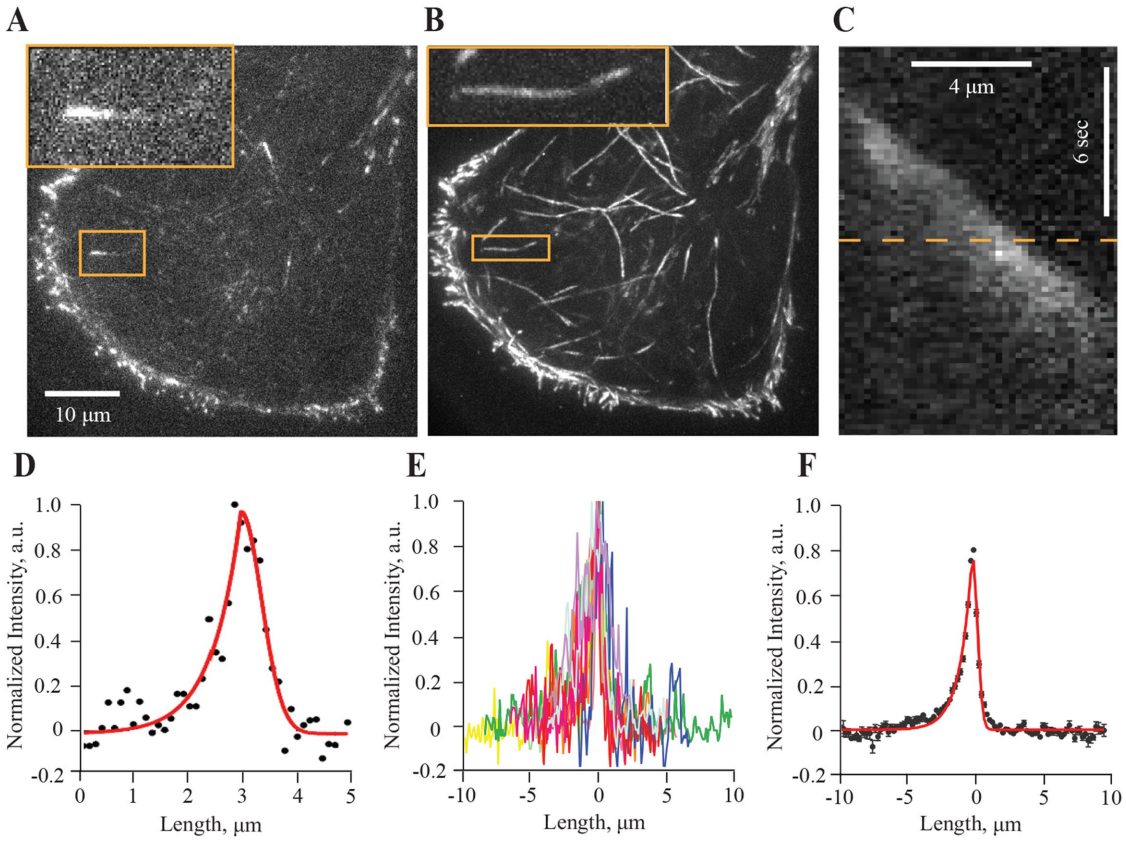

FIGURE 1: Extraction and processing of EB3 profiles. (A) Snapshot of 3T3 fibroblast expressing EB3-RFP comets. Inset zooms into an individual comet. (B) Maximal intensity projection of a stack of frames, visualizing different EB3-RFP tracks. (C) Kymograph of EB3-RFP taken along the track highlighted in yellow in B. (D) Intensity profile along the dashed line of C. Red shows fitting with exponential/Gaussian function. (E) Individual intensity profiles of EB3-RFP aligned by the position of the maximum of the fitting function (see *Materials and Methods*). (F) Averaged EB3-RFP intensity profile fitted with a piecewise exponential/Gaussian function (red).

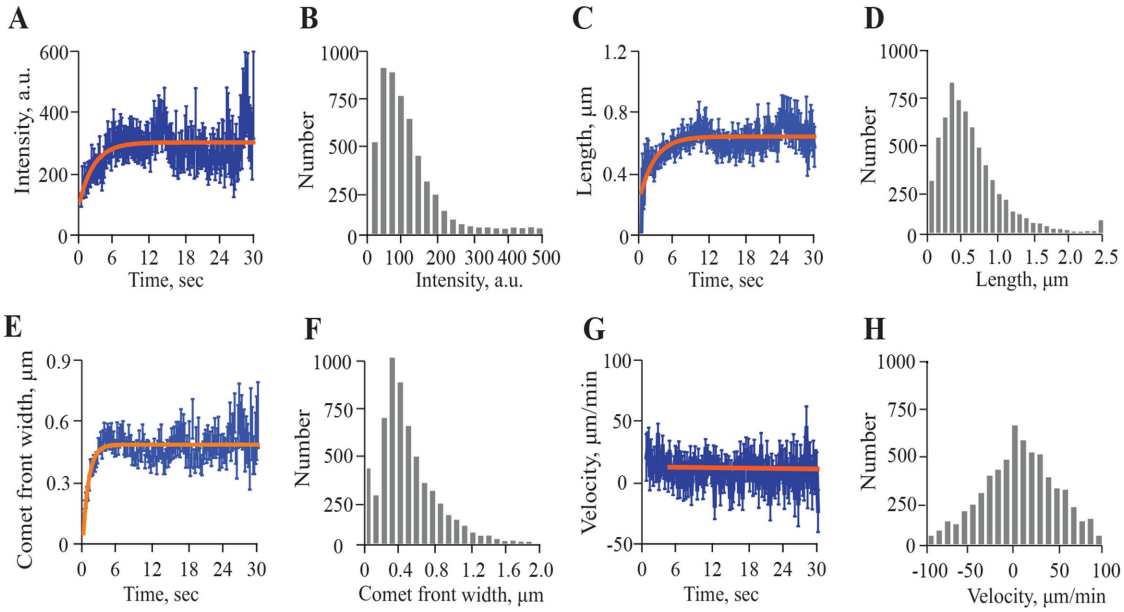

FIGURE 2: Time dependence of EB3 comet characteristics. (A) Amplitude of intensity of EB3-RFP comets as a function of time. The orange line represents data fitted with one-phase association function: $Y = Y_0 + (Y_{plateau} - Y_0) \times (1 - \exp(-Kx))$. (B) Distribution of intensity amplitude values corresponding to all intensity profiles in $N = 120$ kymographs. (C) EB3-RFP comet length as a function of time from comet birth. The orange line represents a fit with one-phase association function like in A. (D) Distribution of EB3-RFP comet lengths corresponding to all intensity profiles in $N = 120$ kymographs. (E) Width of the EB3-RFP comet front (σ) as a function of time. The orange line represents a fit with one-phase association function as in A. (F) Distribution of EB3-RFP comet front width values corresponding to all intensity profiles in $N = 120$ kymographs. (G) Instantaneous MT growth rate as a function of time from comet birth. The orange line is a linear fit. (H) Distribution of instantaneous EB3-RFP comet velocities corresponding to all intensity profiles in $N = 120$ kymographs. Data points in A, C, E, and G represent mean ± SEM.

coefficient, $R^2 = 0.91$ (Figure 1, E and F). Therefore, we have used that approximation to establish average dependences of EB3-RFP profile characteristics on elapsed time from comet "birth" (Figure 2).

EB3-RFP intensity, reached 90% of peak value within 6 s after comet birth (i.e., beginning of the MT plus end growth), and remained relatively constant for the following period of MT elongation (Figure 2, A and B). Length of the EB3-RFP comet reached a 90% of plateau of ~0.6 μm within 8 s (Figure 2, C and D). This plateau value corresponds to ~ 75 layers of GTP/GDP-Pi tubulin dimers, similar to previously published values (Seetapun *et al.*, 2012).

Width of the comet front, described by parameter σ and showing the sharpness of the front of EB3-RFP binding zone, convolved with the point-spread function of RFP, reached 90% of plateau of ~0.5 μm within 2.5 s from the comet birth (Figure 2, E and F). After attaining the plateau, no further continuous increase of the front comet width was observed, suggesting either the lack of MT tapering during its growth or failure of EB3-RFP to decorate tapered MT end. Distribution of instantaneous EB3-RFP comet velocities was broad, containing both positive and negative values, consistent with a previous report (Rickman *et al.*, 2017). Instantaneous EB3-RFP comet velocities showed no statistically significantly change (within 95% confidence interval of the fit) over the period starting 3 s from the comet birth (see Figure 2G). Initial 3-s segment of the curve, characterized by overall higher velocities, was excluded from analysis because of the low signal-to-noise ratio of the EB3-RFP comet during this initial period.

EB3 profiles frequently exhibited stationary EB3-islands

In spite of good approximation of the average EB3-RFP profile by a combination of Gaussian and exponential functions (Figure 1, E and F), we found that many individual profiles significantly deviated from that model. Such deviations could represent either additional complexities in EB3 binding to MTs or could be just due to measurement noise, which is expected to be more pronounced for dim comets, with poor signal-to-background ratio. To clarify that point, we plotted the measure of goodness of fit (determination coefficient R^2) for each profile as a function of EB3-RFP comet intensity amplitude (Supplemental Figure S1). As expected, correlation between poor goodness of fit and low comet intensity was observed, but even for profiles with a high signal-to-noise level, there were substantial and frequent deviations from the empirical model function. Examination of the kymographs, which contained outlier profiles, revealed that they often exhibited secondary EB3-binding zones, besides the leading comet peak (Supplemental Video). The shapes of additional EB3-binding zones were diverse and frequently represented diffuse widening of EB3-RFP comet profile (Figure 3A, brace) or sometimes clear patches of additional EB3-RFP intensity, which we refer to as EB3-islands thereafter (Figure 3, A and B, orange arrowheads).

It is noteworthy that in some cases we also observed fluorescent spots, which were located on growing MTs-free background (Figure 3A, white arrowheads). Those spots, which were obviously distinct from EB3-islands on growing MTs, could potentially contaminate our data. Therefore, we quantified the number of fluorescent spots per unit distance on MTs and on growing MTs-free background in experimental kymographs (Supplemental Figure S2). This revealed significant enrichment of the stationary fluorescent spots on MTs. The validity of the quantification method was additionally verified by its application to analogous simulated kymographs (see Supplemental Figure S2 and *Materials and Methods* for details).

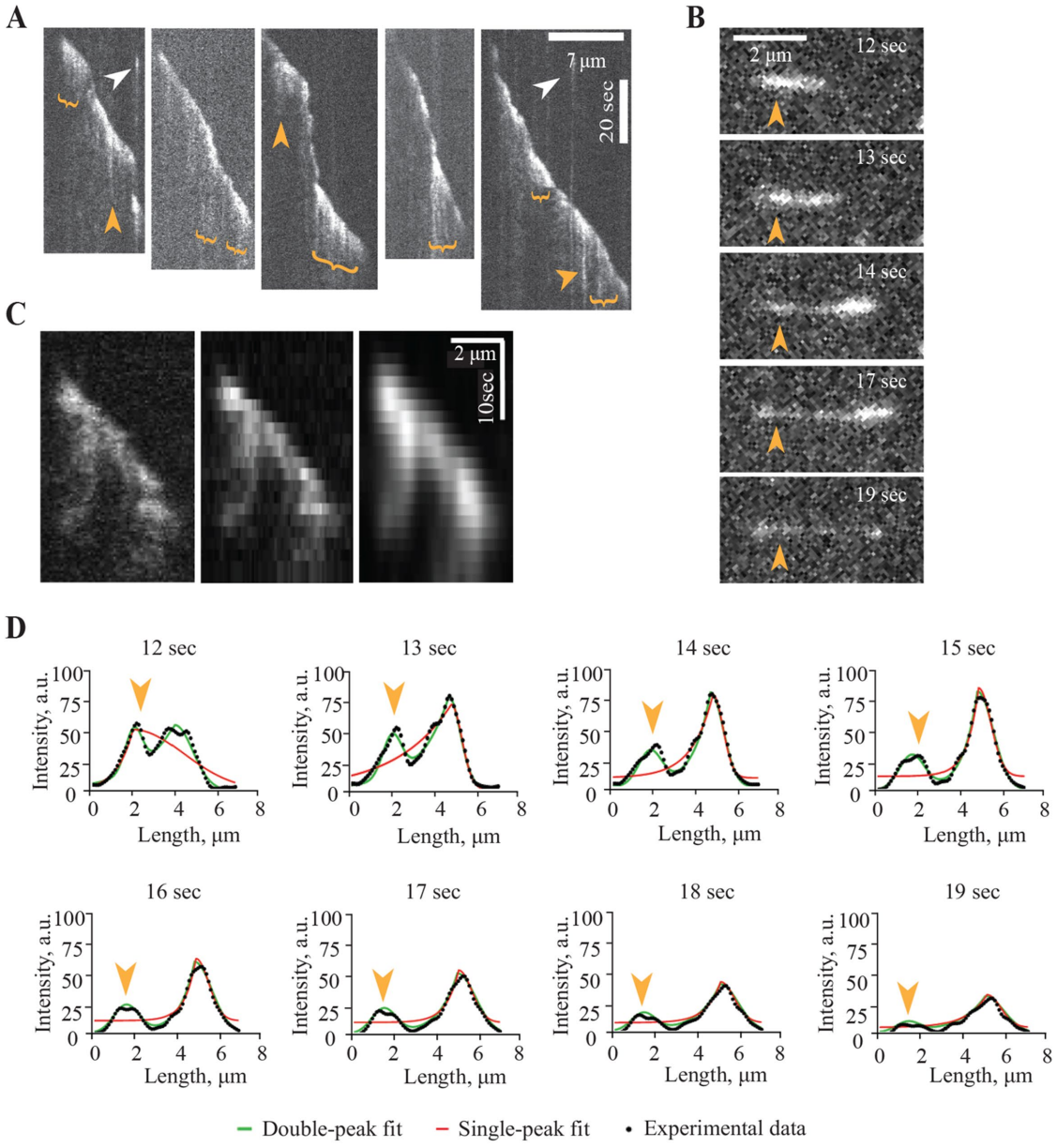

FIGURE 3: Deviation of EB3 profile from exponential shape and identification of EB3-islands on growing MTs. (A) Example of kymographs poorly fitted by piecewise exponential/Gaussian function. Orange arrowheads mark EB3-islands. White arrowhead marks stationary fluorescent spots on MT-free background. (B) Example series of snapshots showing formation of an EB3-island (marked with orange arrowheadsw). The corresponding kymograph is given in the next panel. (C) From left to right: raw kymograph of EB3-RFP on MT, the same kymograph with 1-s binning and binned kymograph smoothed with 2D-Gaussian filter (filter radius = 1.5 pixel). (D) Sequence of profiles from kymograph in C fitted with single-peak exponential-Gaussian function (red) and the double-peak function (green).

The EB3-islands were variable in their lifetimes and intensity, making their automated identification and quantification nontrivial. To facilitate that task, we binned kymographs, averaging each five consecutive frames into one in order to reduce noise. Subsequently, binned kymographs were subjected to 2D Gauss filtering with 1.5 pixel radius (Figure 3C). In the processed kymographs we could unambiguously identify sufficiently large EB3-islands, using automated criteria, as described in detail in *Materials and Methods*. Our approach for EB3-island identification relied on fitting the EB3-RFP intensity profile with a single-peak and multiple-peak functions (Supplemental Figure S3A). If the latter fit happened to be a considerable improvement over a single exponential/Gaussian fit, we defined the profile as containing an EB3-island. One clear example of an EB3-island, identified as a persistent secondary intensity peak, lasting from the 12th second of EB3-RFP comet lifetime until the 19th second, is shown in Figure 3D.

Overall, we quantified 82 EB3-islands on 120 MTs in live fibroblast cells. Durations of the lifespan of EB3-islands were distributed exponentially with half-lifetime of 5.1 s (Figure 4A).

EB3-islands did not follow the main peak of EB3-RFP comet intensity, but rather remained immobile on MTs becoming more distant from the front comet over time (Figure 4B). EB3-islands

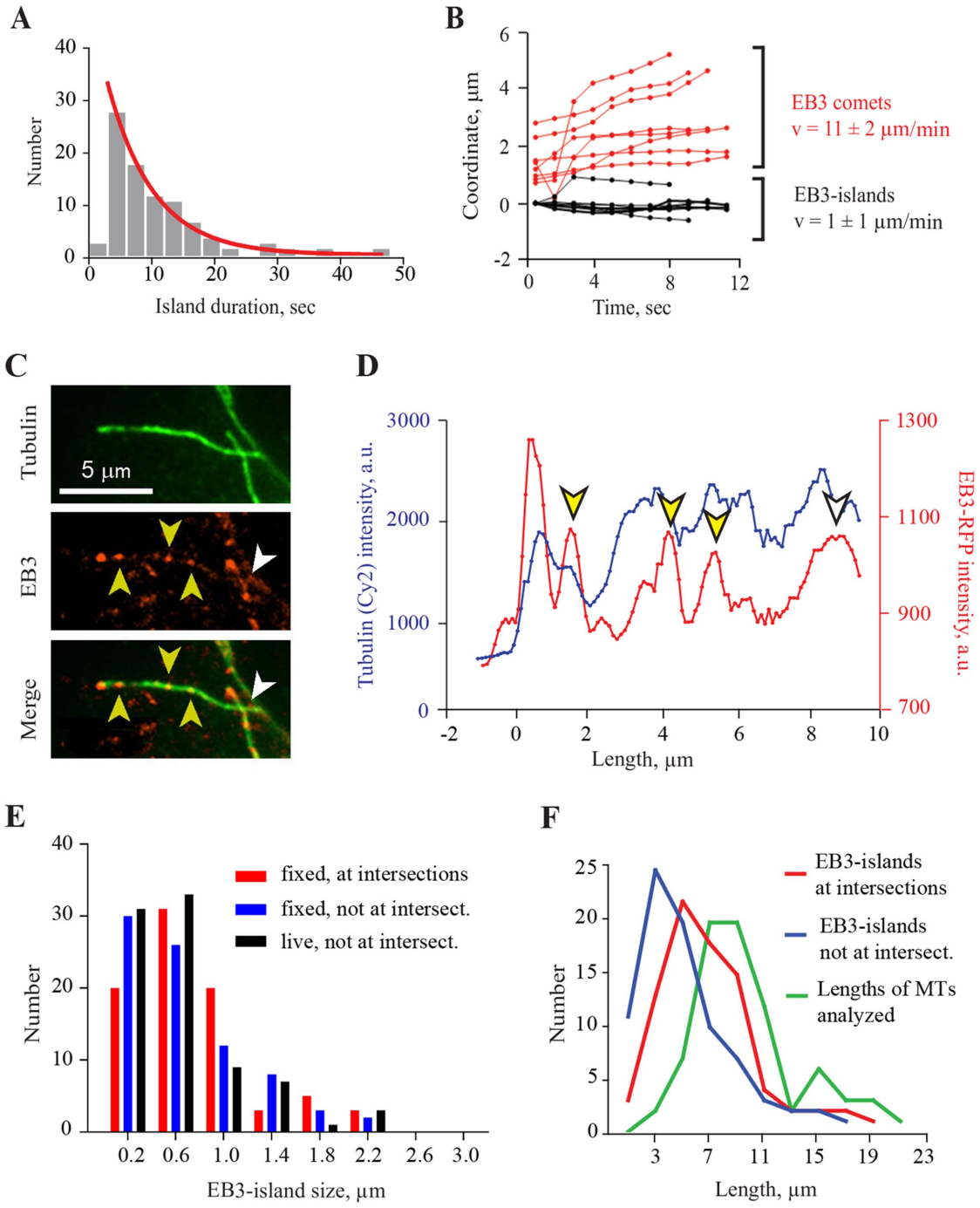

FIGURE 4: Quantification of EB3-islands. (A) Distribution of lifetimes of EB3-islands (gray bars). The red curve is exponential fit. (B) Position vs. time plot for eight representative tracks of EB3-RFP comets (red) and EB3-islands (black) in the same kymographs showing that EB3-RFP comets are moving with the growing MT tip, while the EB3-islands remain static. (C) MT and EB3 seen in separate channels and overlaid. Yellow arrowheads point at EB3-islands outside intersections with MTs; white arrowheads point at EB3-island on MT intersection. (D) Intensity profile of tubulin and EB3 signal along the MT. Arrowheads are colored as in C. (E) Distributions of EB3-island sizes. Red, blue, and black bars correspond to EB3-islands, located at MT intersections in fixed cells, outside MT intersections in fixed cells and in live cells, respectively. (F) Distributions of EB3-island locations relative to the growing MT tip. Red and blue curves correspond to EB3-islands at MT intersections and outside of MT intersections, respectively. The green curve shows distribution of the lengths of MT segments, which were analyzed.

appeared on average once per 44 s of EB3-RFP comet growth time, which corresponded to a spatial frequency of one EB3-island per 9.3 µm of MT length. We did not observe any clear trend in the enrichment of EB3-islands on younger or older comets, suggesting that their appearance was random. Likewise, there was no correlation between the frequency of EB3-islands formation and velocity of the corresponding EB3-RFP comets (Supplemental Figure S3B).

EB3-islands originate from the growing EB3 comets and at MT intersections

In all cases that we observed on relatively short growing MT segments in live cells, EB3-islands originated from the main EB3-RFP comet, rather than arose in a region distant from the growing tip of the MT. However, it has been recently established, that GTP-tubulins can incorporate into MT lattice, and thus they might form additional sites for EB3 binding away from the growing MT tip. For not yet clearly understood reasons, these sites of tubulin exchange often arise at MT intersections (Aumeier *et al.*, 2016; de Forges *et al.*, 2016; Vemu *et al.*, 2018). To estimate fraction of EB3-islands, arising at MT intersections and originating from the growing tip, we fixed the cells, expressing EB3-RFP and immuno-stained them for tubulin. Tubulin staining allowed locating MT crossovers and examining longer MT segments (median MT length of 8.7 μm in fixed vs. 5.4 μm in live cells). Out of 163 islands, which we detected on 76 MTs from 29 fixed cells, 82 (50.3%) were located at MT intersections (Figure 4, C and D, and Supplemental Figure S4, white arrowheads). The rest of the EB3-islands were found outside the MT intersections (Figure 4, C and D, and Supplemental Figure S4, yellow arrowheads). There was no difference in spatial frequency of EB3-islands in live cells and in fixed cells outside of the regions of intersection with other MTs (one island per 9.3 vs. 9.1 μm of MT length, respectively). Sizes of EB3-islands located at MT crossovers and outside of them were not statistically different (Figure 4E). Occurrence of EB3-islands outside of MT intersections was higher near the growing MT tips, as quantified in the Figure 4F. On the basis of this and our live cells imaging data, we propose that EB3-islands, located in the vicinity of the MT tips, predominantly represent stationary EB3-binding zones originating from the growing MT tips.

Average EB3-profile but not EB3-islands can be recapitulated in the computational models with different geometries of EB3-tubulin binding

It is conceivable that the EB3-islands that we observed could arise purely due to the stochastic nature of the GTP hydrolysis/phosphate release. In that scenario, EB3-RFP would mark randomly forming remnants of the GTP/GDP-Pi cap. To test this possibility in a more rigorous manner, we applied a simple and well characterized two-state Monte-Carlo model of MT dynamics (VanBuren *et al.*, 2002). The model was modified to include decoration of the MT with EB3 proteins. The binding site for calponin homology domains of EB-proteins is known to be located in the corner of four tubulin dimers (Maurer *et al.*, 2012; Zhang *et al.*, 2015), but the energetic contribution of each tubulin into EB-protein binding is not yet established. Therefore, we examined several reasonable EB3 binding options: with one, two, or four GTP tubulins sufficient (Figure 5A).

For simplicity, EB3 concentration was assumed to be high enough to saturate all available binding sites on the MT immediately. We kept most of model parameters, responsible for MT dynamics in vivo, as suggested in (Castle *et al.*, 2017). Tubulin concentration was set to be 11 μM, providing ~17 μm/min mean rate MT growth, closely matching our experimental data and consistent with previous estimates of free tubulin concentration in fibroblasts (Hiller and Weber, 1978). EB3 comet length in the model was dependent on GTP hydrolysis constant and the EB3-tubulin binding rule (Figure 5B). However, for each binding rule, it was possible to find a GTP hydrolysis constant value lying roughly in the range of experimental estimates: from 0.085 to 0.3 s^{-1} (O'Brien *et al.*, 1987; Melki *et al.*, 1996).

For consistency between analyses of experimental and simulated data, we generated kymographs of simulated EB3 tracks on growing MTs by convolving the positions of EB3 with a point spread function and added pixel and background noise (Figure 5, C–E). Simulated kymographs were analyzed using the same custom MATLAB scripts, which we had applied to experimental data. This simulation produced EB3 profiles, very well described with our piecewise exponential/Gaussian fitting function (Eq. 2). Secondary peaks of EB3 intensity were virtually never observed in the simulations, irrespective of the EB3 binding rule (see representative profiles in Figure 5, C–E). Hence, we concluded that the EB3-islands could not be explained by stochastic first-order GTP hydrolysis and must have a more complex nature.

Potential origin and role of EB3-islands

Although individual EB comet kymographs in some published reports displayed non-monotonous profiles along MTs (Komarova *et al.*, 2009; Nakamura *et al.*, 2012; Mohan *et al.*, 2013; Roth *et al.*, 2019), to the best of our knowledge, those decoration patterns were not systematically analyzed before. Evidence for stationary EB3-islands on MTs presented in this work indicates that the EB3 binding to MTs in live cells is not yet fully understood. Our computational modeling rules out the simplest of the explanations for EB3-islands. Namely, we argue that random GTP-hydrolysis, leading to appearance of tubulin patches, remaining in GTP-state by pure chance, is not compatible with observed frequency and lifetime of EB3-islands. However, one cannot exclude the possibility that some unknown factors locally slow down GTP hydrolysis in cellular MTs, leading to longer lifetime of some GTP-tubulin patches (Figure 5F). Previously published data suggest that EB3 itself can stimulate nucleotide hydrolysis (Zhang *et al.*, 2015); thus if some additional factors locally prevented EB3 from doing so, a GTP-island would have appeared. Moreover, such GTP-tubulin patches, or GTP-islands, could arise not only due to delayed GTP hydrolysis, but also because of the MT "repair" process. The latter refers to a recently characterized phenomenon of GTP-tubulin exchange between the soluble pool and the MT shaft (Schaedel *et al.*, 2015; Aumeier *et al.*, 2016), which can be additionally enhanced by severing enzymes (Vemu *et al.*, 2018), leading to accumulation of EB-proteins on the freshly incorporated GTP-tubulin lattice. Another possible scenario is that EB3 proteins in the islands are kept bound to the MT because of the action of some unknown protein factor. That factor could act either via forming a complex with multiple EB3 proteins, thereby prolonging their residence time on MTs, or via binding simultaneously to EB3 and tubulin, thus effectively increasing EB3 affinity for MTs.

Despite their catastrophe promoting effects on MT dynamics in purified systems in vitro, EB-proteins conversely stabilize MTs in live cells (Komarova *et al.*, 2009). This activity, likely mediated by EB-binding partners, might lead to promotion of MT rescues by EB3-islands. Indeed, positioned near the growing MT tips, EB3-islands may create an additional stabilization zone, so that MTs, experiencing catastrophes, rescue almost immediately, as shown recently with high-frequency recording of MT dynamics (Guo *et al.*, 2018). Thus, EB3-islands could facilitate small oscillations of MT ends near the cell margin, a behavior which was described previously to be important for high precision targeting of focal adhesions (Krylyshkina *et al.*, 2003). However, further work is required to elucidate the physiological role of EB3-islands in that and potentially other cellular processes.

MATERIALS AND METHODS

Cell culture, transfection, and fluorescence microscopy

NIH-3T3 fibroblasts were maintained in DMEM supplemented with 25 mM HEPES (PanEco, Russia), 10% fetal calf serum (PAA Laboratories, Austria), 2 mM L-glutamine and 0.8 mg/ml gentamicin at 37°C at

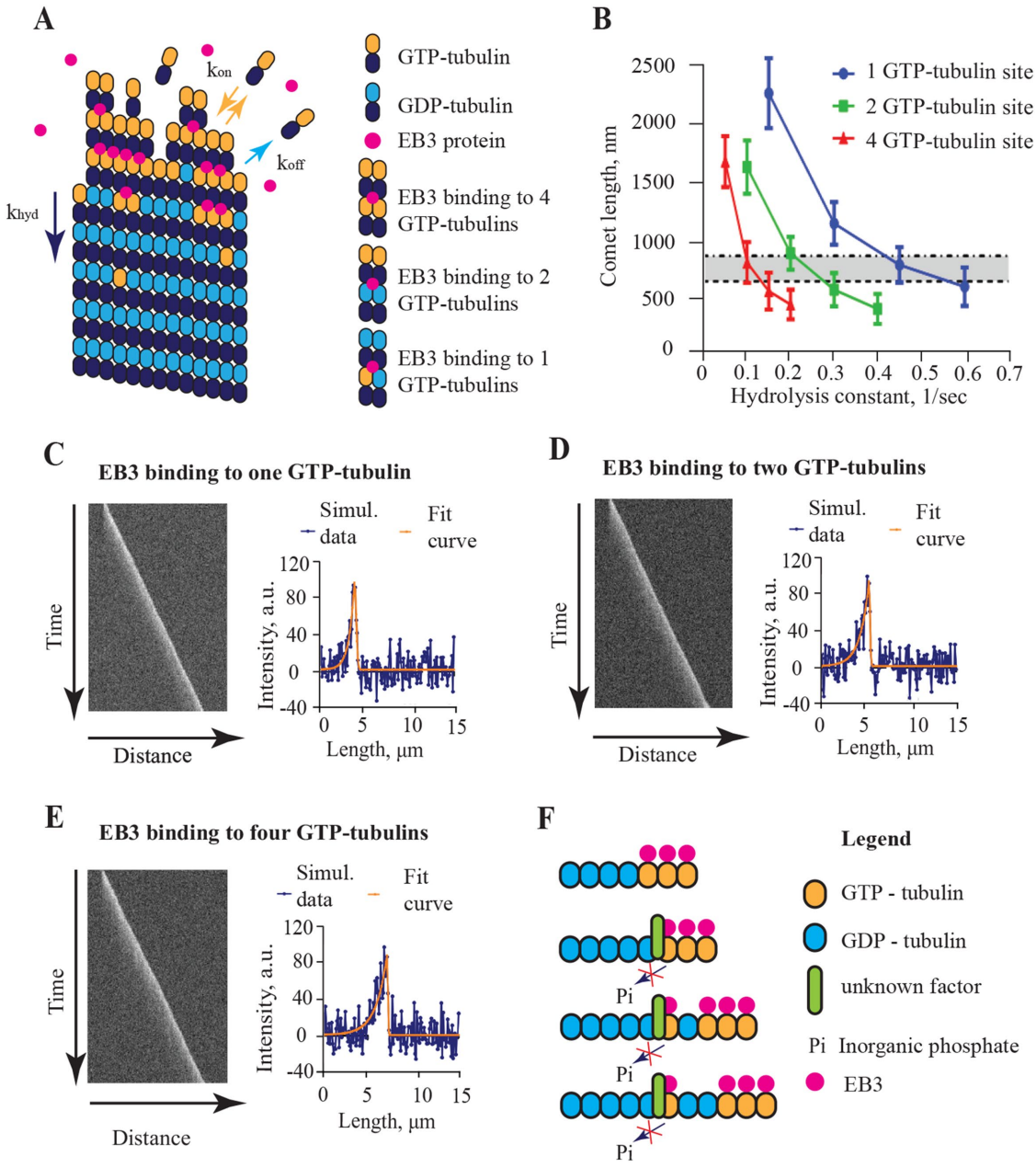

FIGURE 5: Analysis of potential origin of EB3-islands. (A) Schematics of a computational model of growing MT tip decoration with EB3 proteins. (B) Dependence of EB3 comet length in the model as a function of GTP hydrolysis constant. Curves of different colors correspond to different EB3-tubulin binding rules. The gray region between the dotted lines represents the range of experimentally estimated comet length. (C–E) Representative kymographs of EB3 comets in simulations with different GTP hydrolysis constant values and respective representative intensity profiles. Orange is a fit with exponential/Gaussian function. (F) Schematic of the hypothetical mechanism of EB3-island formation.

5% CO_2. Cell suspension obtained with trypsin-EDTA (PanEco, Russia) was plated in 35-mm Petri dishes. The cell density was adjusted so that spreading cells did not contact each other. EB3-RFP gene was cloned into a pGPV lentiviral vector containing copRFP as a reporter and puromycin as drug selection marker (Eurogene, Russia). The lentiviral vector was transduced into HEK293 packaging cells (ATCC # CRL-11268) with XtremeGENE HP DNA transfection reagent according to manufacturer's protocol, viral harvest was collected in 36 and 72 h after transfection and then used for transduction of 3T3 cells. On five separate experimental days, we recorded time-lapse videos of N = 59 NIH-3T3 fibroblast cells on a Nikon TI microscope, equipped with TIRF Apochromat 100×/1.49 oil immersion objective, Andor iXon3 EMCCD camera and 488- and 561-nm lasers. Temperature was kept near 37°C with Bioptech objective heater. Images were recorded every 0.2 s with NIS Elements software. N = 39 of those cells were used for the final kymographs.

Cell fixation and immunostaining. NIH-3T3 fibroblasts with stable expression EB3-RFP protein were fixed with 100% methanol for 15 min at –20°C and washed three times with phosphate-buffered saline (pH 7.2–7.4) for 10 min each. To visualize MTs, cells were stained with antibodies to α-tubulin (mouse, clone DM1A,

Invitrogen, batch#TC2479053) and then stained with secondary goat anti-mouse antibodies conjugated with Cy-2 (Sigma-Aldrich). In both cases, the dilution of antibodies was 1:100; the time of incubation with antibodies was 1 h in 37°C. $N = 60$ cells were recorded for analyses using the same imaging system as for live cells, plus an extra differential interference contrast image was taken for every cell.

Analysis of dynamics of EB3 in live cells

From recorded videos, $N = 120$ EB3-RFP tracks were selected for further analysis, according to the following criteria: 1) EB3-RFP comets should not intersect each other during entire growth period, since the intersection would contribute to the fluorescence intensity of a particular area at a certain time; 2) the moment of appearance of the comet should be clearly observed; 3) EB3-RFP comets should not reach the periphery of the cell, where they merged and became indistinguishable; 4) EB3-RFP comet track is at least 2 μm long. Kymographs of selected EB3-RFP tracks were built in ImageJ and then processed with custom MATLAB scripts.

For each kymograph, the moment of EB3 comet birth was manually defined as a time frame when the EB3-RFP comet became distinguishable from background noise. Intensity profiles of the kymogram for all frames after comet birth were processed as follows. First, the background intensity, determined from the MT-free segment of the kymogram, was subtracted from each intensity profile. Second, each entire intensity profile was fitted with exponential-Gaussian piecewise function in MATLAB:

$$I(x) = \begin{cases} A * e^{\frac{x-x_0}{d}} + B, \; x < x_0 \\ A * e^{-\left(\frac{x-x_0}{\sigma}\right)^2} + B, \; x \geq x_0 \end{cases} \quad (1)$$

Here $I(x)$ is the background-subtracted EB3-RFP fluorescence intensity profile; x is the coordinate along MT; A is the amplitude of fluorescent intensity of the comet; x_0 is a fitting parameter, defined as the coordinate along the comet track, where the maximal intensity is achieved; d is the EB3-RFP comet length parameter; σ is the width of the front of the comet. Outcomes of this fitting were further automatically filtered to exclude clear outliers, such as x_0 outside of the kymograph length, peak intensity below the background noise level, or instantaneous EB3 comet velocity > 200 μm/min.

Identification of EB3-islands on kymographs

To quantify EB3-islands, every five consecutive frames of raw kymographs were averaged into a 1-s frame and then filtered with a 2D Gaussian filter with 1.5-pixel radius. Intensity profiles of processed kymographs were analyzed with an automated EB3-island detecting an algorithm. The algorithm started by fitting each profile with an exponential-Gaussian function (Eq. 1). At the next step, the profile was fitted with a more complex function, containing one additional Gaussian peak:

$$I(x) = \begin{cases} A_0 e^{\frac{x-x_0}{d}} + A_2 e^{-\left(\frac{x-x_2}{\sigma_2}\right)^2}, \; x < x_0 \\ A_0 e^{-\left(\frac{x-x_0}{\sigma_0}\right)^2} + A_2 e^{-\left(\frac{x-x_2}{\sigma_2}\right)^2}, \; x \geq x_0 \end{cases} \quad (2)$$

Here index 0 marks the characteristics of the main EB3 comet peak; A_0, σ_0, and x_0 are its amplitude, front width and position, respectively; while index 2 corresponds to the characteristics of the secondary peak.

EB3-island detection by the algorithm included the following criteria:

1. the profile must have been better fitted with the double-peak function (Eq. 2) than with the single-peak function (Eq. 2), which was formalized with the following criterion:

$$\left(1 - R_{2p}^2\right) \Big/ \left(1 - R_{1p}^2\right) \leq C_{\text{improvement}} \quad (3)$$

where R_{1p}^2, R_{2p}^2 are the determination coefficients of the fits with one-peak and two-peak functions, respectively, and $C_{\text{improvement}}$ is a threshold of fit improvement. To account for the fact that shorter profiles have less space for extra peaks and, thus are more easily fitted, this coefficient scales with profile length, going from 0.5 to 0.8.

2. The intensity amplitude of the second Gaussian peak was greater than 15% of the intensity amplitude of the EB3-RFP comet to be distinguishable from noise.
3. The secondary Gaussian peak should have been well separated from the main EB3-RFP comet peak (see Eq. 2), so that

$$x_0 \geq x_2 + d \quad (4)$$

Analogously, the algorithm then attempted to fit third and fourth Gaussian peaks to the profile to account for the possibility of more than one island being present at a time.

To measure lifetimes of EB3 islands, we applied a grouping algorithm, which was developed to identify EB3-RFP intensity peaks, corresponding to the same EB3-island observed at different time frames of the kymograph. This algorithm defined intensity peaks at different time frames as corresponding to the same EB3 island based on the following criteria: 1) the intensity peaks were distinct from the main EB3 comet; 2) they were located not more than 600 nm from each other; 3) they existed for at least two consecutive seconds. The lifetime of such EB3-islands was defined as the time from the moment when the main EB3-RFP comet has originally passed the location of the island until the time this EB3-island was no longer detected by the algorithm. This portion of the algorithm also automatically recorded the length, lifetime, and average growth rate of the MT segment that has polymerized during this growth event, thus allowing us to quantify directly both spatial and temporal frequency of the EB3-islands.

Quantification of EB3-islands in fixed cells

In fixed cells, a different EB3-island detection algorithm was used to account for the presence of data from tubulin channel and the absence of data on the EB3-island dynamics. At the first step, individual long (>2 μm) MTs with a clearly visible EB3-RFP comet at the end were manually traced in the tubulin channel in ImageJ. Each MT was traced with a segmented line from the plus end for as long as it remained unambiguously visible. Coordinates of the multisegment lines and manually defined positions of MT intersections were then passed into custom fully automated MATLAB script. This script created linescans along each MT in both tubulin and EB3 channels. MT length was calculated as the distance along the linescan segment, where intensity in the tubulin channel was above the lower 10% of intensities of the linescan. EB3-islands were defined as areas of the linescan in the RFP channel, where EB3-RFP intensity was 4 SD above the average intensity of the background intensity level for at least three consecutive pixels. The background area was determined

as the lowest 35th percentile of EB3-RFP intensities along the linescan. The first EB3-RFP peak in each profile was considered to be the main EB3-RFP comet. The second peak and beyond were considered as EB3-islands. The MATLAB script automatically calculated the size of those islands, their positions relative to the plus end of the MT, and whether or not each individual EB3-island was located within an area of intersection with a different MT. When applied to random frames from live cell data, this EB3-island quantification algorithm provided an estimate of the spatial frequency of EB3-island formation, which was consistent with that of the more detailed algorithm, described in Identification of EB3-islands on kymographs above.

Quantification of fluorescent dots on MTs and on MT-free background in kymographs

To evaluate the number of fluorescent spots on MTs and on MT-free background, we developed a semiautomated MATLAB script, which allowed the operator to click on fluorescent stripes and speckles on the kymographs and to define a region corresponding to a MT. Using that input information, the script then calculated the density of fluorescent objects per unit length on MT versus MT-free background. As a control for the script performance, we examined simulated kymographs with stripes and speckles randomly distributed on MTs and beyond (Supplemental Figure S2). As expected, in that case, the algorithm did not reveal any statistically significant difference in the density of spots per unit length on MT versus MT-free background.

Computational modeling

We used a published model of MT dynamics as a starting platform for simulations (Van Buren *et al.*, 2002; Castle *et al.*, 2017). All model parameters were taken as in Castle *et al.* (2017), except for tubulin concentration, which was fine-tuned to provide experimentally observed MT growth rates. To incorporate EB3 into the model, we defined its binding site to be located in the corner of four tubulin dimers. Depending on the EB3-binding rule, one, two, or four tubulin dimers in contact with EB3 were required to be in the GTP-state. We postulated that all binding sites were immediately decorated by EB3 as soon as they were formed. Likewise, EB3 was considered detached as soon as the binding site vanished. EB3 did not decorate GDP-tubulins or incomplete binding sites (lacking at least one of the four tubulin dimers). We did not take into account effects of EB3 on MT dynamics and GTP hydrolysis rate. To simulate kymographs, we convolved EB3 with a Gaussian function with width corresponding to a point spread function of RFP molecule. Then we introduced Gaussian noise with the amplitude, estimated from a MT-free background region of experimental kymographs, and subjected the kymograph to pixelation. Intensity profiles on simulated kymographs were then fitted with piecewise exponential/Gaussian function (Eq. 2) to extract EB3 comet characteristics.

ACKNOWLEDGMENTS

Experimental work and data analyses were supported by the Russian Foundation for Basic Research (Project Nos. 17-54-33009 to I.V. and 18-34-00944 to V.M.) and Grant AP05134232 from Ministry of Education and Science of the Republic of Kazakhstan to I.V. Computational modeling of tubulin and EB3 dynamics was supported by a Russian Science Foundation grant to N.G. (Project # 17-74-20152).

REFERENCES

Akhmanova A, Steinmetz MO (2015). Control of microtubule organization and dynamics: two ends in the limelight. Nat Rev Mol Cell Biol 16, 711–726.

Aumeier C, Schaedel L, Gaillard J, John K, Blanchoin L, Théry M (2016). Self-repair promotes microtubule rescue. Nat Cell Biol 18, 1054–1064.

Bieling P, Kandels-Lewis S, Telley IA, van Dijk J, Janke C, Surrey T (2008). CLIP-170 tracks growing microtubule ends by dynamically recognizing composite EB1/tubulin-binding sites. J Cell Biol 183, 1223–1233.

Bowne-Anderson H, Zanic M, Kauer M, Howard J (2013). Microtubule dynamic instability: a new model with coupled GTP hydrolysis and multistep catastrophe. BioEssays News Rev Mol Cell Dev Biol 35, 452–461.

Brouhard GJ, Rice LM (2018). Microtubule dynamics: an interplay of biochemistry and mechanics. Nat Rev Mol Cell Biol 19, 451–463.

Castle BT, McCubbin S, Prahl LS, Bernens JN, Sept D, Odde DJ (2017). Mechanisms of kinetic stabilization by the drugs paclitaxel and vinblastine. Mol Biol Cell 28, 1238–1257.

de Forges H, Pilon A, Cantaloube I, Pallandre A, Haghiri-Gosnet A-M, Perez F, Poüs C (2016). Localized mechanical stress promotes microtubule rescue. Curr Biol 26, 3399–3406.

Desai A, Mitchison TJ (1997). Microtubule polymerization dynamics. Annu Rev Cell Dev Biol 13, 83–117.

Dimitrov A, Quesnoit M, Moutel S, Cantaloube I, Poüs C, Perez F (2008). Detection of GTP-tubulin conformation in vivo reveals a role for GTP remnants in microtubule rescues. Science 322, 1353–1356.

Duellberg C, Cade NI, Holmes D, Surrey T (2016). The size of the EB cap determines instantaneous microtubule stability. ELife 5, e13470.

Guo Y, Li D, Zhang S, Yang Y, Liu J-J, Wang X, Liu C, Milkie DE, Moore RP, Tulu US, *et al.* (2018). Visualizing intracellular organelle and cytoskeletal interactions at nanoscale resolution on millisecond timescales. Cell 175, 1430–1442.

Hiller G, Weber K (1978). Radioimmunoassay for tubulin: a quantitative comparison of the tubulin content of different established tissue culture cells and tissues. Cell 14, 795–804.

Komarova Y, De Groot CO, Grigoriev I, Gouveia SM, Munteanu EL, Schober JM, Honnappa S, Buey RM, Hoogenraad CC, Dogterom M, *et al.* (2009). Mammalian end binding proteins control persistent microtubule growth. J Cell Biol 184, 691–706.

Krylyshkina O, Anderson KI, Kaverina I, Upmann I, Manstein DJ, Small JV, Toomre DK (2003). Nanometer targeting of microtubules to focal adhesions. J Cell Biol 161, 853–859.

Maurer SP, Bieling P, Cope J, Hoenger A, Surrey T (2011). GTPγS microtubules mimic the growing microtubule end structure recognized by end-binding proteins (EBs). Proc Natl Acad Sci USA 108, 3988–3993.

Maurer SP, Cade NI, Bohner G, Gustafsson N, Boutant E, Surrey T (2014). EB1 Accelerates two conformational transitions important for microtubule maturation and dynamics. Curr Biol 24, 372–384.

Maurer SP, Fourniol FJ, Bohner G, Moores CA, Surrey T (2012). EBs recognize a nucleotide-dependent structural cap at growing microtubule ends. Cell 149, 371–382.

Melki R, Fievez S, Carlier MF (1996). Continuous monitoring of Pi release following nucleotide hydrolysis in actin or tubulin assembly using 2-amino-6-mercapto-7-methylpurine ribonucleoside and purine-nucleoside phosphorylase as an enzyme-linked assay. Biochemistry 35, 12038–12045.

Mohan R, Katrukha EA, Doodhi H, Smal I, Meijering E, Kapitein LC, Steinmetz MO, Akhmanova A (2013). End-binding proteins sensitize microtubules to the action of microtubule-targeting agents. Proc Natl Acad Sci USA 110, 8900–8905.

Mustyatsa VV, Boyakhchyan AV, Ataullakhanov FI, Gudimchuk NB (2017). EB-family proteins: Functions and microtubule interaction mechanisms. Biochem Mosc 82, 791–802.

Nakamura S, Grigoriev I, Nogi T, Hamaji T, Cassimeris L, Mimori-Kiyosue Y (2012). Dissecting the nanoscale distributions and functions of microtubule-end-binding proteins EB1 and ch-TOG in interphase HeLa cells. PLoS One 7.

O'Brien ET, Voter WA, Erickson HP (1987). GTP hydrolysis during microtubule assembly. Biochemistry 26, 4148–4156.

Rickman J, Duellberg C, Cade NI, Griffin LD, Surrey T (2017). Steady-state EB cap size fluctuations are determined by stochastic microtubule growth and maturation. Proc Natl Acad Sci USA 114, 3427–3432.

Roth D, Fitton BP, Chmel NP, Wasiluk N, Straube A (2019). Spatial positioning of EB family proteins at microtubule tips involves distinct nucleotide-dependent binding properties. J Cell Sci 132, jcs219550.

Schaedel L, John K, Gaillard J, Nachury MV, Blanchoin L, Théry M (2015). Microtubules self-repair in response to mechanical stress. Nat Mater 14, 1156–1163.

Seetapun D, Castle BT, McIntyre AJ, Tran PT, Odde DJ (2012). Estimating the microtubule GTP cap size in vivo. Curr Biol 22, 1681–1687.

VanBuren V, Odde DJ, Cassimeris L (2002). Estimates of lateral and longitudinal bond energies within the microtubule lattice. Proc Natl Acad Sci USA 99, 6035–6040.
Vemu A, Szczesna E, Zehr EA, Spector JO, Grigorieff N, Deaconescu AM, Roll-Mecak A (2018). Severing enzymes amplify microtubule arrays through lattice GTP-tubulin incorporation. Science 361, eaau1504.
Zakharov PN, Arzhanik VK, Ulyanov EV, Gudimchuk NB, Ataullakhanov FI (2016). Microtubule: a dynamically unstable stochastic phase switching polymer. Uspekhi Fiz Nauk 186, 853–868.
Zhang R, Alushin GM, Brown A, Nogales E (2015). Mechanistic origin of microtubule dynamic instability and its modulation by EB proteins. Cell 162, 849–859.